LES of turbulent non-isothermal two-phase flows within a multifield approach

Solène Gouénard, Stéphane Vincent, Stephane Mimouni

LES of turbulent non-isothermal two-phase flows within a multifield approach*

LES des écoulements diphasiques turbulent anisothermes par une approche de modélisation multi-champs

Solène Gouénard[1], Stéphane Vincent[2], Stéphane Mimouni[3]

[1] CEA CESTA, Le Barp, France, solene.gouenard@cea.fr
[2] Université Paris-Est Marne-La-Vallée, UMR CNRS 8208, Laboratoire de Modélisations et Simulation Multi-Echelle, Marne-la-Vallée, France, stephane.vincent@u-pem.fr
[3] Electricité de France, R&D Division, Chatou, France, stephane.mimouni@edf.fr

ABSTRACT. Safety issues in nuclear power plant involve complex turbulent bubbly flows. To predict the behavior of these flows, the two-fluid approach is often used. Nevertheless, this model has been developed for the simulation of small spherical bubbles, considered as a dispersed field. To deal with bubbles with a large range of sizes, a multifield approach based on this two-fluid model has been proposed. A special treatment, called the Large Bubble Model (LBMo), has been implemented and coupled to the dispersed model. However, only laminar and isothermal flows were considered in previous papers. Thus, here, Large Eddy Simulations (LES) are investigated to model turbulence effects. For this purpose, the two-fluid model equations are filtered to highlight the specific subgrid terms. Then, an *a priori* LES study using filtered Direct Numerical Simulation (DNS) results is detailed. This analysis allows classifying these terms according to their relative weight and then concentrating the modelling efforts on the predominant ones. Five different turbulence models are compared. These results are finally used to perform true LES on a turbulent two-phase flow. Moreover, in order to tackle non-isothermal flows occurring in industrial studies, a new heat transfer model is implemented and validated to deal with phase change at large interfaces using the Large Bubble Model.
KEYWORDS. Two-phase flows, Multifield approach, Two-fluid model, Large interfaces, Large Eddy Simulation, Phase change.

Introduction

Turbulent non-isothermal flow studies with Computational Multi-Fluid Dynamics (CMFD) tools require the ability of dealing with not only inclusions of different sizes and shapes but also turbulence effects and phase change. To deal with the first issue, two approaches can be considered. Bubbly flows occurring in nuclear power plants or in conventional heat exchangers are often modelled with an Eulerian dispersed description within the two-fluid model of Ishii [1975]. In this model, the bubbles are small enough to be considered spherical. Thus, interfacial forces such as drag force, lift force, wall lubrication, virtual mass and turbulent dispersion force are implemented [*e.g.*, Mimouni *et al.* 2011]. However, this approach is not suitable for the simulation of large and deformable bubbles. In the second type of approaches, inclusions are located using interface tracking methods such as Front-Tracking [*e.g.*, Unverdi and Tryggvason 1992], Level-Set [*e.g.*, Sussman *et al.* 1994] or Volume Of Fluid (VOF) [*e.g.*, Hirt and Nichols 1981]. Nevertheless, to simulate flows containing inclusions of different sizes, the grid has to be refined according to the smallest interfacial scale. In industrial configurations, these methods are not sustainable in terms of Central Processing Unit (CPU) consumption.

More recently, new categories of methods have been developed by combining the two previous approaches for the simulation of flows containing inclusions with a large range of sizes. In the first type of

* The results presented in this paper have been obtained with the CMFD tool NEPTUNE_CFD, developed in the framework of the MULTIPATH project, financially supported by CEA (Commissariat l'Énergie Atomique et aux Energies Alternatives), EDF (Électricité de France), IRSN (Institut de Radioprotection et de Sûreté Nucléaire) and AREVA NP, in collaboration with the MSME laboratory (Université Paris-Est Marne-la-Vallée, Champs sur Marne, France). The authors are grateful for access to the computational facilities of the french CINES (National computing center for higher education) and CCRT (National computing center of CEA) under project number x20172b6115.

approaches, the larger scales are simulated using interface tracking methods described above and the badly resolved structures are considered as dispersed particles followed by a Lagrangian method. This has been implemented by several research groups with the Level-Set method [*e.g.*, Capecelatro *et al.* 2010 and Herrmann 2010] and with the VOF method [*e.g.*, Tomar *et al.* 2010 and Ling *et al.* 2015]. A second type of approach, called the multifield approach, has been introduced a long time ago by Anderson and Jackson [1967] and Drew and Lahey [1979]. Contrary to the first method, the multifield approach is based on a two-fluid model initially used to simulate complex flows containing a continuous phase and spherical inclusions modelled through a dispersed approach. It has been implemented by different research groups with a Lagrangian description of the small spherical inclusions [*e.g.*, Zuzio *et al.* 2013] and with Eulerian methods [*e.g.*, Vallet and Borghi 1999 and Lebas *et al.* 2009]. In this article, this second type of approach based on an Eulerian description of the smallest inclusions is used. The two-fluid model is then adapted for the simulations of large and deformable inclusions by considering a second continuous field in the balance equations. The large inclusions are considered as an interface between two continuous fields whereas the small spherical inclusions are treated as a dispersed field. Specific treatments are required to simulate these interfaces, which are referred as the Large Bubble Model (LBMo). This model has been extensively validated on laminar isothermal flows in previous papers [*e.g.*, Denèfle *et al.* 2015 and Fleau *et al.* 2015]. The criteria to switch from the large interfaces treated with the LBMo to the dispersed field and the opposite are not given in this paper since we will focus on the large interfaces. Readers are invited to refer to Mimouni *et al.* [2017] for details. However, industrial studies require the ability of dealing with both turbulence and phase change effects.

Thus, the second main issue in complex turbulent flows, considered in this paper, is the turbulence modelling in presence of interfaces. Within the multifield approach, large interfaces are described in a deterministic way through the volume fraction, updated in the mass balance equation. Therefore, to simulate turbulent flows, Large Eddy Simulation (LES) seems more suitable since it is also based on a deterministic description of the turbulence effects. The simulation of turbulent two-phase flows containing large interfaces has never been performed with two-fluid models. However, a lot of work have been done in single-fluid models to analyze the subgrid terms, quantify them and compare different turbulence models [*e.g.*, Labourasse *et al.* 2007, Vincent *et al.* 2008 and Larocque *et al.* 2010]. Thus, in this article, it is proposed to follow the same methodology applied to single-fluid models to the two-fluid model with the LBMo.

Finally, the third issue consists in the treatment of phase change at large interfaces using the Large Bubble Model. Different phase change models are available in the literature. The most widely used is the model proposed by Lee [1980], based on an empirical expression to quantify the interfacial heat and mass transfer term. Nevertheless, a coefficient has to be fixed to bring the temperature of the cells containing the interface close to the saturation temperature. A large range of values has been obtained in the literature from 0.1 s^{-1} [*e.g.*, Wu *et al.* 2007, Schepper *et al.* 2009 and Alizadehdakhel *et al.* 2010] to 100 s^{-1} [*e.g.*, Yang *et al.* 2008 and Fang *et al.* 2010]. It has also been shown that too large values could induce numerical instabilities with oscillations of the temperature around the saturation temperature. To avoid the issue of fixing an empirical coefficient, the development of a formulation based on theoretical considerations is necessary. Thus, to estimate the heat flux jump at the interface, the Fourier's law is applied. This model and other similar approaches have been used by several research groups [*e.g.*, Mao 2009, Nichita and Thome 2010, Kunkelmann *et al.* 2012, Ganapathy *et al.* 2013 and Sun *et al.* 2014] with VOF or Level-Set method. Nevertheless, all these models are applied to interfaces contained in one grid cell. In the framework of the multifield approach with the two-fluid model, the large interfaces are diffused over a few cells. The expression of the heat flux has to be adapted to interfaces with a non-zero thickness. Thus, the development, implementation and validation of a new heat transfer model based on the methodology proposed by Brackbill *et al.* [1992] for the surface tension force is detailed.

After presenting the computational model, an *a priori* LES study will be performed to evaluate the order of magnitude of the subgrid terms appearing in the filtered two-fluid model equations and to compare different turbulence models usually applied to single-phase flows. For this purpose, the phase inversion benchmark [*e.g.*, Vincent *et al.* 2016] will be simulated. Then, the more suitable turbulence model will be

assessed on a horizontal pipe of water and air. The objective of this test case is to highlight the ability of the code to predict flow regimes. This last point is crucial in nuclear power plants to improve the performance and the life span of pipes. Finally, non-isothermal flows will be considered. A new phase change model for large interfaces will be implemented and validated.

Nomenclature

Greek letters:			Subscripts and superscripts:	
$\Delta\tau$	s	Characteristic time scale	$\overline{}$	LES filter
ξ	-	Convergence order	i, j	Space directions
Δx	m	Cube root of the cell volume	I	Cell index
ρ	$kg.m^{-3}$	Density	k	Field index
μ	$kg.m^{-1}.s^{-1}$	Dynamic viscosity	v	Vapor phase
$\hat{\Delta}$	m	Filter width	l	Liquid phase
κ	m^{-1}	Interface curvature	Int	Interface
Γ	$kg.m^{-3}.s^{-1}$	Interfacial mass transfer		
ϵ	-	Relative error		
λ	$W.m^{-1}.K^{-1}$	Thermal conductivity		
χ	$m^2.s^{-1}$	Thermal diffusivity		
σ	$N.m^{-1}$	Surface tension coefficient		
Ω	m^3	Volume of a cell		
ε^*	-	Volume fraction		

Roman letters:			Acronyms:	
C_p	$J.m^{-1}.K^{-1}$	Specific heat capacity	ADM	Approximate Deconvolution Model
d_p	m	Characteristic length scale	CSF	Continuum Surface Force
g	$m.s^{-2}$	Gravity acceleration	CMFD	Computational Multi-Fluid Dynamics
G	-	LES filter	CPU	Central Processing Unit
h	-	Heaviside function	DNS	Direct Numerical Simulation
H	$J.kg^{-1}$	Enthalpy	LBMo	Large Bubble Model
I_d	-	Identity matrix	LES	Large Eddy Simulation
L	$J.kg^{-1}$	Latent heat	VOF	Volume Of Fluid
n	-	Unit interface normal vector	WALE	Wall-Adapting Local Eddy-Viscosity
P	Pa	Pressure		
Q	$W.m^2$	Conductive thermal flux		
S	s^{-1}	Viscous stress tensor		
T	K	Temperature		
u	$m.s^{-1}$	Velocity		

Computational model

In this section, the two-fluid model is presented in the context of large and deformable interfaces. The balance equations are solved for each field. Thus, in the framework of the multifield approach, for a two-phase flow with water and steam inclusions of different sizes, three fields are considered: a continuous liquid field, a continuous gas field (contained in the large deformable steam inclusions) and a dispersed gas field (the small spherical steam inclusions). Then, the Large Bubble Model, implemented for the simulation of interfaces between two continuous fields, is detailed.

Two-fluid model The code NEPTUNE_CFD is based on an Eulerian approach with a finite volume discretization. The flow motion is followed using the two-fluid model of Ishii [1975] extended to n-phase. In this model, the density, the viscosity and the local velocity are defined for each field in each cell. The following governing equations are solved for each field k:

- The mass balance equation:

$$\partial_t \varepsilon_k^* \rho_k + \partial_{x_i}\left(\varepsilon_k^* \rho_k u_{i,k}\right) = \Gamma_k \tag{1}$$

With ε_k^* the volume fraction of field k, ρ_k its density, $u_{i,k}$ the ith component of the velocity of field k and Γ the mass transfer term.

- The momentum balance equation in each space direction i:

$$\begin{aligned}\partial_t(\varepsilon_k^* \rho_k u_{i,k}) + \partial_{x_j}\left(\varepsilon_k^* \rho_k u_{i,k} u_{j,k}\right) = \mu_k \partial_{x_j}\left(\varepsilon_k^* S_{ij,k}\right) - \varepsilon_k^* \partial_{x_j} P \\ + \varepsilon_k^* \rho_k g_i + F_{i,k}\end{aligned} \tag{2}$$

Where μ_k denotes the viscosity of field k, S the viscous stress tensor, P the pressure, g the gravitational constant and $F_{i,k}$ the specific source terms depending on the field (continuous or dispersed).

- The energy balance equation:

$$\begin{aligned}\partial_t(\varepsilon_k^* \rho_k H_k) + \partial_{x_j}\left(\varepsilon_k^* \rho_k H_k u_{j,k}\right) \\ = -\partial_{x_j}(\varepsilon_k^* Q_{j,k}) + \mu_k \partial_{x_j}\left(\varepsilon_k^* \mu_k S_{ij,k} u_{j,k}\right) \\ + \varepsilon_k^* \partial_t P + \varepsilon_k^* \rho_k g_i u_{i,k} + E_k^{Int}\end{aligned} \tag{3}$$

With H_k the total enthalpy, $\boldsymbol{Q}_k = -\lambda_k \nabla T_k$, the conductive thermal flux, λ_k the thermal conductivity and T_k the temperature, E_k^{Int}some other interfacial energy transfers. The energy balance equation is only solved when non-isothermal flows are considered, which will be only done in the last section.

In the code NEPTUNE_CFD, the assumption of a common pressure for all fields is made.

The simulations are performed on fixed grids with collocated variables. The data structure is totally face-based, which allows the use of arbitrary-shaped cells including non-conforming meshes [*e.g.*, Guelfi *et al.* 2007]. The well-known Semi-Implicit Method for Pressure-Linked Equations (SIMPLE) solver is used in the CMFD tool [*e.g.*, Patankar and Spalding 1972]. An iterative coupling of the equations is implemented to ensure mass and energy conservation.

Large Bubble Model The Large Bubble Model [*e.g.*, Denèfle *et al.* 2015 and Fleau *et al.* 2015] has been developed to simulate large interfaces with a two-fluid model. This model consists in three elements necessary for an accurate simulation of large and deformable inclusions.

Surface tension. The surface tension model used in the code NEPTUNE_CFD for the simulation of the large interfaces corresponds to the volumetric formulation [*e.g.*, Bartosiewicz *et al.* 2008, Denèfle

et al. 2015 and Fleau *et al.* 2015] of the Continuum Surface Force (CSF) model proposed by Brackbill *et al.* [1992]:

$$\boldsymbol{F_{CSF}} = \varepsilon_k^* \sigma \kappa \nabla \varepsilon_k^* \Omega \tag{4}$$

With σ the surface tension coefficient, Ω the cell volume and κ the local curvature:

$$\kappa = -\nabla . \left(\frac{\nabla \varepsilon_k^*}{||\nabla \varepsilon_k^*||} \right) \tag{5}$$

This surface tension force appears in the momentum balance equation applied to continuous fields through the term $F_{i,k}$.

Drag force. In the two-fluid model, the drag force is crucial. Contrary to the single-fluid approach, two different velocities are defined, one for each field. The role of the drag force law is to couple these two velocities at the interface. Thus, a new drag force expression has been developed to deal with large interfaces within the multifield approach [*e.g.*, Fleau *et al.* 2015]:

$$\begin{cases} \varepsilon_2^* < 0.3 : & \mathbf{F_{bubble}} = \varepsilon_1^* \varepsilon_2^* \dfrac{18\mu_1}{\varepsilon_1^* d_p^2} (\boldsymbol{u_1} - \boldsymbol{u_2}) \\ \varepsilon_2^* > 0.7 : & \mathbf{F_{droplet}} = \varepsilon_1^* \varepsilon_2^* \dfrac{18\mu_2}{\varepsilon_2^* d_p^2} (\boldsymbol{u_1} - \boldsymbol{u_2}) \\ 0.3 \leq \varepsilon_2^* \leq 0.7 : & \mathbf{F_{mix}} = \dfrac{0.7 - \varepsilon_2^*}{0.7 - 0.3} \mathbf{F_{bubble}} + \dfrac{\varepsilon_2^* - 0.3}{0.7 - 0.3} \mathbf{F_{droplet}} \end{cases} \tag{6}$$

The characteristic length scale d_p is equal to $\sqrt{\frac{\mu_2}{\mu_1}} \frac{\varepsilon_k^*}{||\nabla \varepsilon_k^*||}$ close to the large interfaces, for $0.1 \leq \varepsilon_1^* \varepsilon_2^* \leq 0.25$, and to the diameter of the dispersed bubbles/droplets far from them, for $\varepsilon_1^* \varepsilon_2^* \leq 0.02$. Between these two regions, a linear extrapolation of these two values is defined.

This drag force appears in the momentum balance equation applied to continuous fields through the term $F_{i,k}$.

Interface sharpening. To control the interface thickness, the interface sharpening equation proposed by Olsson and Kreiss [2005] and adapted to the two-fluid formulation is solved for each continuous field [Fleau *et al.* 2016]:

$$\partial_\tau \varepsilon_k^* + \nabla . (\varepsilon_k^* (1 - \varepsilon_k^*) \boldsymbol{n}) = K \Delta \varepsilon_k^* \tag{7}$$

With $\boldsymbol{n} = \frac{\nabla \varepsilon_k^*}{||\nabla \varepsilon_k^*||}$ the interface normal vector. The values of the parameters $\Delta\tau = \frac{\Delta x}{32}$ and $K = \frac{\Delta x}{2}$ (Δx denotes the cell size) are chosen to obtain a final interface thickness always equal to 5 cells whatever the initial interface diffusion [*e.g.*, Štrubelj 2009 and Denèfle *et al.* 2015].

The LBMo has been widely validated on various isothermal test cases [*e.g.*, Duponcheel, *et al.* 2016, Fleau *et al.* 2015, Fleau *et al.* 2016, Mimouni *et al.* 2017 and Vincent *et al.* 2016]. Reasonable

agreements have been obtained with analytical and experimental data on free surface and bubble test cases in laminar and turbulent conditions.

Filtered two-fluid equations

As previously done in Labourasse *et al.* [2007] and Vincent *et al.* [2008] with the single-fluid model and Lakehal [2004] with the two-fluid model including a dispersed field, the LES filter is applied to the two-fluid model equations for two continuous fields within the LBMo. In this section, the flows are considered isothermal. Thus, the filtered energy balance equation is not detailed. No dispersed fields are taken into account.

The filtered mass balance equation:

$$\rho_k \partial_t \overline{\varepsilon_k^*} + \rho_k \nabla . \left(\overline{\varepsilon_k^*}\, \overline{u_{i,k}} \right) + \tau_{interf} = 0 \tag{8}$$

With $\overline{\varepsilon_k^*}$ the filtered volume fraction of field k and τ_{interf} a subgrid term related to the relationship between the filtered velocity $\overline{u_{i,k}}$ and the interface topology (see Table 1).

The filtered momentum balance equation:

$$\begin{aligned} \rho_k \partial_t \left(\overline{\varepsilon_k^*}\, \overline{u_{i,k}} \right) + \tau_{time} + \rho_k \nabla . \left(\overline{\varepsilon_k^*}\, \overline{u_{i,k}}\, \overline{u_{j,k}} \right) + \tau_{conv} \\ = \mu_k \nabla . \left(\overline{\varepsilon_k^*}\, \overline{S_k} \right) + \tau_{diff} - \overline{\varepsilon_k^*} \nabla \overline{P} - \tau_{pressure} \\ + \overline{\varepsilon_k^*} \rho_k g_i + \widehat{F_{CSF}} + \tau_{superf} + \widehat{F_{drag}} + \tau_{drag} \end{aligned} \tag{9}$$

With τ_{time}, τ_{conv}, τ_{diff} the time, convective and diffusive subgrid terms and $\tau_{pressure}$, τ_{superf} and τ_{drag} three specific subgrid terms of the two-fluid model applied to two continuous fields (see **Error! Reference source not found.**1 for the expressions). τ_{drag} has the following expression:

$$\tau_{drag} = \overline{F_{drag}} - \widehat{F_{drag}} \tag{10}$$

With $\overline{F_{drag}}$ defined as:

$$\begin{aligned} \overline{\varepsilon_2^*} < 0.3 : \quad & \overline{\mathbf{F_{bubble}}} = \overline{\varepsilon_1^* \varepsilon_2^* \frac{18\mu_1}{\varepsilon_1^* d_p^2} (\boldsymbol{u_1} - \boldsymbol{u_2})} \\ \overline{\varepsilon_2^*} > 0.7 : \quad & \overline{\mathbf{F_{droplet}}} = \overline{\varepsilon_1^* \varepsilon_2^* \frac{18\mu_2}{\varepsilon_2^* d_p^2} (\boldsymbol{u_1} - \boldsymbol{u_2})} \\ 0.3 \le \overline{\varepsilon_2^*} \le 0.7 : \quad & \overline{\mathbf{F_{mix}}} = \overline{\frac{0.7 - \varepsilon_2^*}{0.7 - 0.3} \mathbf{F_{bubble}} + \frac{\varepsilon_2^* - 0.3}{0.7 - 0.3} \mathbf{F_{droplet}}} \end{aligned} \tag{11}$$

And $\widehat{F_{drag}}$:

$$\overline{\varepsilon_2^*} < 0.3 : \quad \widehat{\mathbf{F_{bubble}}} = \overline{\varepsilon_1^*}\,\overline{\varepsilon_2^*}\frac{18\mu_1}{\overline{\varepsilon_1^*}\widehat{d_p}^2}(\overline{\boldsymbol{u_1}} - \overline{\boldsymbol{u_2}})$$

$$\overline{\varepsilon_2^*} > 0.7 : \quad \widehat{\mathbf{F_{droplet}}} = \overline{\varepsilon_1^*}\,\overline{\varepsilon_2^*}\frac{18\mu_2}{\overline{\varepsilon_2^*}\widehat{d_p}^2}(\overline{\boldsymbol{u_1}} - \overline{\boldsymbol{u_2}}) \qquad (12)$$

$$0.3 \leq \overline{\varepsilon_2^*} \leq 0.7 : \quad \widehat{\mathbf{F_{mix}}} = \frac{0.7 - \overline{\varepsilon_2^*}}{0.7 - 0.3}\widehat{\mathbf{F_{bubble}}} + \frac{\overline{\varepsilon_2^*} - 0.3}{0.7 - 0.3}\widehat{\mathbf{F_{droplet}}}$$

$\widehat{F_{CSF}}$ can be written in the same way as $\widehat{F_{drag}}$ by applying the LES filter at each quantity. We can notice that, compared to the one-fluid model, specific subgrid terms appear in the filtered two-fluid model equation, which are $\tau_{pressure}$, τ_{drag}. Thus, seven subgrid terms have to be modeled (see Table 1).

A priori les study

After presenting the filtered equations and the specific subgrid terms appearing, the phase inversion benchmark is simulated with the LBMo to perform an *a priori* LES study. Only continuous fields are considered for this simulation. This test case is turbulent and isothermal. A validation of the results can be found in Vincent *et al.* [2016]. In this analysis, the value of the volume fractions, pressure and velocities are filtered. This allows classifying the subgrid terms according to their weight. Then, turbulence models are applied and compared.

Presentation of the test case In this test case, an oil drop with a cubic shape (size of L/2) is initially placed in a cubic box (size L = 0.1 m) containing liquid water (see Figure 1). The evolution of the system is driven by the gravity forces in the z direction (g = 9.81 m.s^{-2}). At the end of the simulation, the oil phase is supposed to be located in the top part of the box with the liquid water beneath. The fluid properties are given in Table 2. Interfacial tension coefficient between oil and water is equal to 0.045 N.m^{-1}.

The test case has been simulated with three different mesh refinements: 128^3 cells, 256^3 cells and 512^3 cells. The time steps are kept constant and are respectively equal to 0.8 ms, 0.2 ms and 0.05 ms such that the CFL number is constant and always smaller than 0.9. The simulations have been performed with 144 cores for the first grid and 1152 for the two others during respectively 7 hours, 47 hours and 2 months and a half to reach 13 physical seconds.

Order of magnitude of the subgrid terms The subgrid terms appearing in the filtered two-fluid equations are compared in terms of order of magnitude to find the predominant and negligible ones. This first step is important since the larger the contribution of this subgrid term is, the more the modelling errors will impact the simulation. For this purpose, a uniform box filter is applied to the simulation results extracted at the peak of enstrophy (maximum value of the velocity curl) for the three grids. Only the first neighborhood of each cell (filter size of 2) is considered. The subgrid term τ_{time} is not represented in this study since the analysis is proposed only for one time. Each subgrid term in the momentum balance equation is normalized by the convection resolved term. The interfacial subgrid term τ_{interf} appearing in the mass balance equation is normalized by its corresponding resolved part. The summation of the subgrid term and the convection (resp. interfacial) resolved term is made in the whole domain, only where the phase is present, as illustrated here with the convection subgrid term:

$$\overline{\tau_{conv}} = \frac{\sum_{\overline{\varepsilon_k^*}^I > 1 \cdot 10^{-10}} \left| \overline{\tau_{conv}}^I \right|}{\sum_{\overline{\varepsilon_k^*}^I > 1 \cdot 10^{-10}} \left| \rho_k \nabla . \left(\overline{\varepsilon_k^*}^I \, \overline{u_{i,k}}^I \, \overline{u_{j,k}}^I \right) \right|} \qquad (13)$$

The results are presented in Figure 2. Table 3 proposes a classification of the subgrid terms according to the phase for the most refined grid. As documented in Labourasse *et* al. [2007], Vincent *et al.* [2008] and Larocque *et al.* [2010], the subgrid term τ_{superf} is largely predominant for the two phases. Furthermore, a small contribution of the diffusion subgrid term τ_{diff} is observed for the two phases. Nevertheless, for the oil phase, contrary to the single-fluid formulation, this contribution is not negligible and very close to those of τ_{conv} and τ_{interf} . The results obtained with the single-fluid formulation seem to be closer to those obtained here for the water phase.

As expected also, the magnitude of each subgrid term decreases when the mesh is refined except τ_{superf} for the oil phase. This increase has been previously observed with single-fluid formulations [*e.g.*, Vincent *et al.* 2016]. In the two-fluid model formulation, this evolution is the result of two opposite effects:

- The first effect is related to the ratio between the numerical and the laminar viscosities of each phase. When the mesh is refined, the velocities increase since the numerical viscosity decreases. The water phase is more sensitive to a variation of the numerical viscosity since its laminar viscosity is smaller. Thus, the velocities in the water phase increase more than in the oil phase, which has a larger laminar viscosity. The resolved convection term increase then more in the water phase than in the oil phase.
- The second effect is the number of small inclusions which increases when the mesh is refined and induces an increase of the subgrid term.

The evolution of the subgrid term contribution depends then on which effect is predominant. For the oil phase, it seems that the increase of small inclusions drive the evolution of the subgrid term, whereas for the water phase, the decrease of the numerical viscosity is predominant.

Finally, the contribution of the drag subgrid term τ_{drag} is not mentioned in Figure 2 for the sake of clarity. Its order of magnitude is largely higher than the contribution of the other subgrid terms. It would require more specific attention in future works.

Comparison of turbulence models After identifying the predominant terms, a comparison of different turbulence models is proposed. Five models are compared: the Smagorinsky's model [*e.g.*, Smagorinsky 1963], the Wall-Adapting Local Eddy-Viscosity (WALE) model [*e.g.*, Nicoud and Ducros 1999], the Bardina's model [*e.g.*, Bardina *et al.* 1980], the Approximate Deconvolution Model (ADM) [*e.g.*, Adams and Stolz 2002] and the mixed Smagorinsky-Bardina's model [*e.g.*, Bardina *et al.* 1983]. ADM is taken with an order of 6. This choice will be discussed here after.

For this comparison, the relative error of each model is evaluated using the L2 norm:

$$\epsilon_{conv}^{ADM} = \sqrt{\frac{\sum_{\overline{\varepsilon_k^*}^I > 1 \cdot 10^{-10}} \left(\overline{\tau}_{conv}^{DNS} - \overline{\tau}_{conv}^{ADM} \right)^2}{\sum_{\overline{\varepsilon_k^*}^I > 1 \cdot 10^{-10}} \left(\overline{\tau}_{conv}^{DNS} \right)^2}} \qquad (14)$$

Figure 3 presents these relative errors for each model and each subgrid term with the most refined mesh. Since the Smagorinsky's and the WALE models are mainly based on consideration about kinetic energy and inertial effects in turbulent flows, they can only be applied to τ_{conv} and τ_{interf}. This figure highlights that ADM is the most appropriate model for all the subgrid terms whatever the phase [*e.g.*, Vincent *et al.* 2016]. However, for the water phase, the error level of ADM applied to the pressure

subgrid term remains high. This has a limited effect since the pressure term is not predominant, as shown in the previous section.

Figure 4 left displays the dispersion and the slope obtained between each model and the filtered DNS results for the convective subgrid term. ADM is the only model to present a slope close to 1 with a limited dispersion.

No data have been given in Figure 3 for the drag subgrid term since the error is always higher than 100 %. As shown in Figure 4 right, this is probably due to the region splitting of the drag force expression, which induces a deviation of the modeled subgrid term at the boundaries [*e.g.*, Sagaut and Germano 2005 and Carrara and DesJardin 2008]. A solution to model this subgrid term could be to adapt the phase-conditioned filtering proposed by Trontin *et al.* [2012] for the velocity and stress tensor jump at interfaces to the regions defined in the drag force expression.

To assess this assumption, a derivative expression of the drag force without region splitting is tested:

$$\mathbf{F_{mix}} = \frac{1}{2}\varepsilon_1^*\varepsilon_2^*\left(\frac{18\mu_1}{\varepsilon_1^* d_{pbubble}^2} + \frac{18\mu_2}{\varepsilon_2^* d_{pdroplet}^2}\right)(\boldsymbol{u_1} - \boldsymbol{u_2}) \qquad (15)$$

With $d_{pbubble} = \sqrt{\frac{\mu_2}{\mu_1}}\frac{\varepsilon_2^*}{||\nabla\varepsilon_2^*||}$ and $d_{pdroplet} = \sqrt{\frac{\mu_2}{\mu_1}}\frac{\varepsilon_1^*}{||\nabla\varepsilon_1^*||}$.

This drag force is not suitable for the simulation of three fields but can be a first approximation in case of two continuous field simulations such as in the phase inversion benchmark. With this derivative expression, the error for ADM decreases from more than 100 % with the splitting version to 69 % with the non-splitting one and the most refined mesh.

To finish with the model comparison, the ability of each turbulence model to reproduce the effective viscosity predicted by DNS is studied. For this purpose, the equivalent viscosity, whose expression is given in Equation (16), is compared with the turbulent viscosity of each model defined in Equation (17).

$$\mu_{eq} = \varepsilon_1^*\frac{\overline{\tau}_{conv1}^{DNS} : \nabla\overline{\boldsymbol{u_1}}}{\overline{S_1} : \nabla\overline{\boldsymbol{u_1}}} + \varepsilon_2^*\frac{\overline{\tau}_{conv2}^{DNS} : \nabla\overline{\boldsymbol{u_2}}}{\overline{S_2} : \nabla\overline{\boldsymbol{u_2}}} \qquad (16)$$

$$\mu_{ADM} = \varepsilon_1^*\frac{\overline{\tau}_{conv1}^{ADM} : \nabla\overline{\boldsymbol{u_1}}}{\overline{S_1} : \nabla\overline{\boldsymbol{u_1}}} + \varepsilon_2^*\frac{\overline{\tau}_{conv2}^{ADM} : \nabla\overline{\boldsymbol{u_2}}}{\overline{S_2} : \nabla\overline{\boldsymbol{u_2}}} \qquad (17)$$

The results for the Smagorinsky's model and ADM are displayed in Figure 5 for the most refined mesh (512^3 cells). The equivalent viscosity can be negative especially close to interfaces. This observation has been previously made by Labourasse *et al.* [2007]. The Smagorinsky's model is unable to reproduce these negative contributions and the other variations observed along the box height. On the contrary, a good agreement is obtained with ADM.

ADM order In all these comparisons, ADM with an order of 6 has been used since it corresponds to the best results obtained with the *a priori* LES study of the test case using a single-fluid approach [e.g., Tavares *et al.* 2016]. However, in this section, a comparison of the relative error for the convection term and the deconvolution error on the velocity field is proposed according to the ADM order. The error for the convection term is evaluated using Equation (14) and the deconvolution error with:

$$\epsilon_{u_k}^{ADM} = \sqrt{\frac{\sum_{\overline{\varepsilon_k^*}^I > 1 \cdot 10^{-10}} \left(\overline{\boldsymbol{u}}_k^{DNS} - \overline{\boldsymbol{u}}_k^{ADM}\right)^2}{\sum_{\overline{\varepsilon_k^*}^I > 1 \cdot 10^{-10}} \left(\overline{\boldsymbol{u}}_k^{DNS}\right)^2}} \tag{18}$$

The results are given in Figure 6 for the three grids. Contrary to the single-fluid formulation, if the order is increased, the accuracy is not automatically increased. There is an optimal value. Under this value, the increase of the order improves the deconvolution of the velocity field and so the relative errors decrease.

However, when the order is increased after this optimal value, the ADM approximation of the velocity includes values of the considered field in cells belonging to a far neighborhood. The flow in this far neighborhood can be quite different from the cell of interest. This decorrelation has a negative effect and thus increases the deconvolution error. The optimal order is obtained when an equilibrium is reached between the positive effect of the order increase on the deconvolution approximation and the negative effect of the decorrelation of the cells in the far neighborhood. For the convection term, this optimal value is equal to 4. We can note that the conclusions are the same if we are considering another subgrid term. Concerning the deconvolution error, the best order is equal to 3 for the three grids. Finally, we see that the deconvolution error is very small compared to the ADM error of the subgrid terms (see Figure 3). This error decreases with the mesh refinement, which means that the more refined the mesh is, the better the velocity field is approximated by ADM whatever its order.

Effect of the filter In this section, an analysis of the filter choice is proposed. The previous box filter (Equation (19)) is compared to a Gaussian filter (Equation (20)).

$$G(x) = \frac{1}{\hat{\Delta}} h\left(\frac{\hat{\Delta}}{2} - |x|\right) \tag{19}$$

With h the Heaviside function and $\hat{\Delta}$ the filtered width equal to $2\Delta x$ for the two filters.

$$G(x) = \sqrt{\frac{6}{\pi \hat{\Delta}^2}} exp\left(\frac{-6x^2}{\hat{\Delta}^2}\right) \tag{20}$$

Figure 7 displays a comparison of the subgrid term weight according to the filter. Table 4 orders the term according to their contribution with the Gaussian filter and has to be compared to Table 3. The weight of the subgrid terms τ_{superf}, τ_{conv} and τ_{diff} decreases with the Gaussian filter whereas it increases for τ_{interf} and $\tau_{pressure}$. Globally, the subgrid terms contribution is then smaller. This is an important result since if a subgrid term has a limited contribution in the balance equations, the errors made by modeling it will have a limited impact. Thus, it can be appropriate to prefer a filter which limits the contribution of the subgrid terms.

Then, the turbulence models are compared with the two filters in Figure 8 for the oil phase. The same results are obtained with the water phase. The filter has no effect on the Smagorisnky's and WALE models. These results were expected since these models are not strongly linked to the filter choice contrary to the Bardina model and ADM. For these two models, the relative error decreases when the Gaussian filter is applied except for the pressure subgrid term. Once again, the results are in agreement with the expectations. Indeed, in practice, applying a filter corresponds to evaluating a quantity regarding to its value over few cells. With a box filter with a filter size of 2, the filtered quantity is evaluated by averaging all the values over the cells with at least a common node with the cell of interest. The surrounding cells are considered with the same weight. However, with the

Gaussian filter, the same cells are considered but they are weighted according to the distance from the cell of interest. This approach seems better since the flow in the cells far from the cell of interest can be quite decorrelated from the flow in the cell of interest. This difference can large enough to induce deconvolution errors and modelling inaccuracies.

The Gaussian filter seems then better than the box filter since the contribution of the subgrid terms is globally smaller and the modelling errors are reduces.

According to the results presented in this section, in what follows, ADM is implemented with an order of 3 using a Gaussian filter.

Comparison of turbulence models with true LES

In the previous section, LES studies have been performed using filtered DNS. Thus, here, true LES are presented on a two-phase flow using the multifield approach.

Presentation of the METERO experiment The METERO experiment has been jointly developed in the framework of the NEPTUNE project by CEA, EDF, AREVA and IRSN in order to improve numerical CMFD tools by contributing to model validations. This experiment allows establishing a flow pattern map in Figure 9 according to the injection mass flow rate of water and air. The objective of the study is to show that LES modelling coupled with the multifield approach allows predicting qualitatively and quantitatively the readjusted flow regimes. A first ADM simulation is also performed on this test case as a preliminary study.

Presentation of the test case. The experiment consists in a horizontal cylindrical pipe (see Figure 10 for the schematic view), in which water and air can be injected at the same time with different mass flow rates (from 0 $m.s^{-1}$ to 5 $m.s^{-1}$ for water and from 0 $m.s^{-1}$ to 0.7 $m.s^{-1}$ for air). The air injection tubes have been set to ensure uniform bubble injection in the inlet section. The test section is 5.4 m long for an inner diameter of 0.1 m. The flow properties are extracted at three different positions along the pipe. Further informations on the experiment can be found in [*e.g.*, Bottin *et al.* 2014].

Simulation results. The simulations of the experiment have been performed with a cylindrical mesh containing 966168 cells (see Figure 11). The boundary conditions are standard: inlet on the right, outlet on the left and walls everywhere else. The properties of the two phases are presented in Table 5. Surface tension coefficient is equal to 0.075 $N.m^{-1}$. The simulations are performed until they reach 13 s including 5 s of averaging.

Comparison between RANS and LES In the first study, the air velocity at the injection is fixed at 0.127 $m.s^{-1}$. Three liquid velocities are simulated 4.42 $m.s^{-1}$, 2.65 $m.s^{-1}$ and 1.59 $m.s^{-1}$ corresponding respectively (according to Figure 9) to a stratified bubble flow, plug flow and slug flow. The time steps are given in Table 6. For these three simulations, the multifield approach is used. Thus, the small spherical bubbles are treated using the dispersed model. LBMo is activated for the large deformable bubbles. Three fields are defined: a continuous liquid field, a continuous gas field and a dispersed gas field. Isothermal transfer (break up and coalescence) between the two gaseous fields are allowed [*e.g.*, Mimouni *et al.* 2016]. The turbulence models are only applied to the liquid field. Figure 12 presents the qualitative comparison of the simulation results performed with the WALE model. When the liquid velocity decreases, the bubble are supposed to become larger. Thus, the number of bubbles treated as a dispersed field decreases. The simulation results correlate with these experimental observations. Then, in Figure 13, the WALE model is quantitatively compared to the RANS approach. The prediction of the liquid velocity and the void fraction are improved by the use of a LES model. This result was also expected since the RANS approach is based on an ensemble average description of turbulence effects. In flows containing only small spherical bubbles treated with a dispersed approach, this view is suitable. However, when large interfaces are resolved, the deterministic description intrinsically brought by LES modelling is more appropriate.

ADM implementation To finish, a last simulation is performed with ADM. For this purpose, the slug flow test case (J_L = 1.59 m.s^{-1} and J_G = 0.127 m.s^{-1}) is simulated considering only two continuous fields. For this simulation, the ADM order is equal to 3 and reduced close to walls. A Gaussian filter is used. To model the relaxation term [*e.g.*, Schlatter *et al.* 2004], the dynamic Smagorinsky's model is applied [*e.g.*, Germano *et al.* 1991]. Moreover, a new definition is given for the filtered velocity. Indeed, in the two-fluid model, the velocity of a field k is defined in the whole domain even if in one cell the field k is not present. In such cells, the value of the velocity of field k has no meaning and can be criticized. Thus, the following expression of the velocity is used for the filtering process:

$$\overline{\boldsymbol{u}}_k^{NEW} = \frac{\overline{\varepsilon_k^*}\,\overline{\boldsymbol{u}_k}}{max(\overline{\varepsilon_k^*}, 1\cdot 10^{-4})} \qquad (21)$$

With this expression, the smaller the volume fraction is, the smaller the velocity weight is in the filtering process.

To reconstruct the volume fractions with ADM, a treatment is also made to correct the obtained values such that the reconstructed volume fraction is between 0 and 1, which is not intrinsically ensured by the ADM process. Indeed, the reconstructed volume fraction as the following expression:

$$\overline{\varepsilon_k^*}^{ADM} = \sum_{l=0}^{N} (I_d - G)^l * \overline{\varepsilon_k^*} \qquad (22)$$

With N the ADM order, I_d the identity matrix, G the LES filter and $*$ the convolution operator. With this expression, a simple analysis based on the barycentre theory shows that $\overline{\varepsilon_k^*} \in [0;1]$ does not imply that $\overline{\varepsilon_k^*}^{ADM} \in [0;1]$. However, if $\sum_k \overline{\varepsilon_k^*} = 1$, then $\sum_k \overline{\varepsilon_k^*}^{ADM} = 1$.

For this purpose, the negative value of $\overline{\varepsilon_k^*}^{ADM}$ are multiplied by -1. If $\overline{\varepsilon_{k1}^*}^{ADM}$ is negative, its value is multiplied by -1 and $\overline{\varepsilon_2^*}^{ADM}$ is readjusted such that $\overline{\varepsilon_1^*}^{ADM} + \overline{\varepsilon_2^*}^{ADM} = 1$. This point is a major uncertainty in our implementation of ADM that would require further considerations. Finally, in a first attempt, only τ_{conv}, τ_{superf} and τ_{diff} are modeled.

The results, displayed in Figure 13, are encouraging. Indeed, they are not so far from the experimental data. Errors are probably made by considering only two continuous fields. It has to be noted that no discrepancies have been observed concerning mass conservation since only $\overline{\varepsilon_k^*}^{ADM}$ was modified. The mass balance equation is solved considering $\overline{\varepsilon_k^*}$ which does not receive any special treatment. Moreover, in this first implementation, the subgrid term τ_{interf} appearing in the mass balance equation has not been modeled.

In future works, all the choices made for the simulation should be assessed. Moreover, extension to three field simulations should be done.

New phase change model for large interfaces

In the previous sections, the objective has been the investigation of LES to simulate the turbulence effects. Turbulence is a main issue for the simulation of complex flows evolving in nuclear power plants or in conventional heat exchangers. However, phase change has also a major impact. Within the multifield approach implemented in the framework of the two-fluid model, large interfaces are treated with the Large Bubble Model. Nevertheless, the approach does not include a model in case of phase change at the interface. Thus, in this section, a model for the heat flux is proposed to deal with the phase change effects occurring at large interfaces.

Implementation of the new heat flux model To obtain the new heat flux model, the same methodology proposed by Brackbill *et al.* [1992] for the surface tension force is used. For this purpose, we consider an interface with a zero thickness, represented in red in Figure 14. For such interfaces, the heat flux expression for the liquid phase is:

$$q_l^S = \lambda_l \nabla T_l . \boldsymbol{n} \tag{23}$$

For the demonstration here, only the liquid term is considered. Nevertheless, the same process can be followed to obtain the volume reformulation of the vapor term. As done for the surface tension model, the volume expression of the heat fluxes q_l^V corresponding to an interface with a thickness equal to h can be obtained by considering:

$$\lim_{h\to 0} \int_{V^{Int}} q_l^V(x) dx^3 = \int_{A^{Int}} q_l^S(x^{Int}) dA \tag{24}$$

with V^{Int} the volume of an interface with a thickness equal to h and A^{Int} the area of a zero thickness interface. To obtain the expression of $q_l^V(x)$, the definition of $q_l^S(x^{Int})$ is used:

$$\begin{aligned} \int_{A^{Int}} q_l^S(x^{Int}) dA &= \int_{V^{Int}} q_l^S(x) \delta(\boldsymbol{n}(x^{Int}).(x - x^{Int}) dx^3 \\ &= \int_{V^{Int}} \lambda_l \nabla T_l(x).\boldsymbol{n}(x) \delta(\boldsymbol{n}(x^{Int}).(x - x^{Int}) dx^3 \end{aligned} \tag{25}$$

With δ a Dirac function indicating interface.

In Brackbill *et al.* [1992], the interface is located with a color function C, using a VOF approach. Thus, by introducing the notations of this article, we can write the following relation between the color function gradient of the diffused interface and the normal vector $\boldsymbol{n}$:

$$\lim_{h\to 0} \nabla C(x) = \boldsymbol{n}(x) \delta(\boldsymbol{n}(x^{Int}).(x - x^{Int})[C] \tag{26}$$

With $[C]$ the jump of the color function over the interface. Using this expression, we obtain:

$$\int_{A^{Int}} q_l^S(x^{Int}) dA = \lim_{h\to 0} \int_{V^{Int}} \lambda_l \nabla T_l(x) \frac{\nabla C(x)}{[C]} dx^3 \tag{27}$$

Therefore, the volume expression of the heat flux $q_l^V(x)$, with the color function C, is:

$$q_l^V(x) = \lambda_l \nabla T_l(x) \frac{\nabla C(x)}{[C]} \tag{28}$$

In the two-fluid formulation, as previously done for the surface tension model, this expression is rewritten:

$$q_k^V(x) = \varepsilon_k^* \lambda_k \nabla T_k(x) \nabla \varepsilon_k^*(x) \tag{29}$$

With $\nabla T_k(x) = \frac{T_{sat} - T_k(x)}{d^{Int}}$ and d^{Int} the distance to the interface.

Validation of the new heat transfer model To validate the new heat transfer model, two test cases involving steam and water are simulated. In all these simulations, the interface motion is only driven by heat transfer. Mesh sensitivity is also studied for each test case.

Sucking problem. In the sucking problem, steam and liquid water are contained in a 1D tube with a heated wall (see Figure 15). The liquid is superheated at T_{max} and the wall temperature is fixed at $T_{wall} = T_{sat}$ so that steam is at the saturation temperature (see Figure 16). Therefore, there is no temperature gradient in the vapor. Both fields are at the rest at t = 0 s. For t > 0 s, the liquid begins to boil at the interface, which induces a displacement of the steam/water interface.

The theory of the sucking problem is given in Welch and Wilson [2000]. First, let us make a transformation of the spatial coordinates such as the steam/water is located at $\xi = 0$:

$$\xi = x - \int_0^t v_S(t')dt' \tag{30}$$

With v_S the interface velocity. With this new coordinate, the temperature profile is given by:

$$T = T_{sat} + B\sqrt{\frac{\pi}{2}}\phi'(0)\, exp(x_0^2)\, erf(x_0, x) \tag{31}$$

With $B = \frac{\chi_l \rho_l}{C\rho_v}$, $C = \frac{\lambda_l}{L\rho_v}$, χ_l being the thermal diffusivity of the liquid phase, L the latent heat between steam and liquid water, $x = \frac{\eta + \phi'(0)}{\sqrt{2}}$, $x_0 = \frac{\phi'(0)}{\sqrt{2}}$, $\eta = \frac{\xi}{\sqrt{2\chi_l t}}$ and $erf(x_0, x) = \frac{2}{\sqrt{\pi}}\int_{x_0}^{x} \exp(-t^2)\, dt$ the error function. The evolution of the interface position has the following expression:

$$X(t) = \frac{\phi'(0)\rho_l}{\rho_v}\sqrt{2\chi_l t} \tag{32}$$

$\phi'(0)$ can be obtained by solving the following equation:

$$\phi'(0) exp\left(\frac{\phi'(0)^2}{2}\right) = \sqrt{\frac{2}{\pi}}\frac{T_{max} - T_{sat}}{B} \tag{33}$$

The study is based on Sato's and Welch's publications [*e.g.*, Sato and Niceno 2013, Welch and Wilson 2000]. The physical properties of steam and water are updated at each time step using the standard set of thermodynamic Equations Of State based on CATHARE functions [*e.g.*, Emonot *et al.* 2011]. The pressure of the system is equal to $1.013 \cdot 10^5$ Pa (the atmospheric pressure) and the liquid temperature in the bulk is $T_{max} = 378.15\ K$.

The tube length is equal to 2 cm. A heated wall boundary condition ($T_{wall} = T_{sat}$) is imposed on the left face, an outlet boundary condition on the right face and symmetry planes everywhere else (see Figure 15). The liquid temperature is initialized by using Equation (31) at t = 0.1 s. Therefore, the interface position at the beginning of the simulation is compared to the theoretical position at t = 0.1 s. Four different mesh refinements have been used with cell sizes equal to: $1 \cdot 10^{-4}$ m, $5 \cdot 10^{-5}$ m, $2.5 \cdot 10^{-5}$ m and $1.25 \cdot 10^{-5}$ m. The time step is kept constant and fixed according to the grid to ensure a constant Fourier number in all the simulations. The time steps are respectively equal to $1.6 \cdot 10^{-3}$ s, $4 \cdot 10^{-4}$ s, $1 \cdot 10^{-4}$ s and $2.5 \cdot 10^{-5}$ s.

For the initialization, steam is defined in the first four cells. The five next cells are composed with a mixture of the two phases and the rest of the domain is mom with liquid. The five mixed cells have the following composition in steam: 87.5 % for the first one, 75 %, 50 %, 25 % and 12.5 %. This initialization is consistent with the 5 cells interface thickness imposed by the interface sharpening equation.

To compare the analytical solution with the simulation results, special care has to be taken concerning the interface and the temperature profile position. Indeed, in the analytical view of the test case (see Figure 17), the interface has a zero thickness and the temperature jump corresponds to the interface position. In the simulation, the temperature jump begins where the liquid is present, that is to say at one extremity of the interface (see Figure 17). In the post-processing procedure, the position of the interface is taken where $\varepsilon_v^* = \varepsilon_l^* = 0.5$ corresponding to the centre of the smeared interface. Since we consider that the analytical interface position corresponds to the position of the temperature jump, we have to shift the simulated results. Thus, an initial time onset is evaluated using the analytical expression of the interface position over time and taking the analytical interface position at 0.1 s (the temperature profile is initialized at 0.1 s) decreased by $2.5\Delta x$ (5 cells thickness). The simulated results are shifted using this time onset. Moreover, the interface position at 0.1 s in all the curves is considered as the zero position.

The results are given in Figure 18. The more refined the mesh is, the closer to the analytical solution the results are. The results obtained with the most refined mesh are very close to the analytical results. This confirms the ability of the developed model to predict an interface motion only driven by the heat transfer term. Figure 19 presents the corresponding average relative error for the interface position between 0.1 s and 1.5 s. When the mesh is refined, the error decreases. This study allows defining the order of convergence ξ (using the Richardson's extrapolation (31)) equal to 1.1.

$$\xi = \frac{ln\left(\frac{X_{m_3} - X_{m_2}}{X_{m_2} - X_{m_1}}\right)}{ln\left(\frac{1}{2}\right)} \tag{34}$$

with m_1, m_2 and $m_3$three mesh refinements, such as:

$$\Delta x_{m_3} = \frac{\Delta x_{m_2}}{2} = \frac{\Delta x_{m_1}}{4} \tag{35}$$

Stefan problem. The Stefan problem is very close to the sucking problem. Steam and liquid water are contained in a 1D tube with a heated wall under atmospheric pressure. But, in this case, steam is superheated and the liquid water temperature is equal to the saturation temperature $T_{sat} = 373.15\ K$. The wall temperature keeps a constant value during the simulation: $T_{wall} = 398.15\ K$. As a consequence, there is a temperature gradient in the vapor phase (see Figure 20).

The evolution of the interface position is given by the equation [*e.g.*, Welch and Wilson 2000]:

$$X(t) = 2\beta\sqrt{\chi_v t} \tag{36}$$

The temperature profile is equal to:

$$T(x,t) = T_{wall} + \frac{T_{sat} - T_{wall}}{erf(\beta)}\ erf\left(\frac{x}{2\sqrt{\chi_v t}}\right) \tag{37}$$

β is the solution of the equation:

$$\beta\ exp(\beta^2)\ erf(\beta) = \frac{C_{pv}(T_{wall} - T_{sat})}{\sqrt{\pi}L} \tag{38}$$

With C_{pv} the specific heat capacity of vapour.

The physical properties of steam and water are updated at each time step using the standard set of thermodynamic Equations Of State based on CATHARE functions [*e.g.,* Emonot *et al.* 2011]. The pressure of the system is equal to $1.013 \cdot 10^5$ Pa. The same grids have been used with the same boundary conditions. The only difference is the wall temperature which is equal to 398.15 K, that is to say $T_{sat} + 25\ K$, in the Stefan problem instead of T_{sat} in the sucking problem. Three different mesh refinements have been used with cell sizes equal to: $1 \cdot 10^{-4}$ m, $5 \cdot 10^{-5}$ m and $2.5 \cdot 10^{-5}$ m. The time steps are respectively equal to $1.6 \cdot 10^{-3}$ s, $4 \cdot 10^{-4}$ s and $1 \cdot 10^{-4}$ s.

The volume fractions are initialized as previously done with the sucking problem. The initial vapor temperature is approximated using an affine function:

$$T_v(x) = T_{wall} + \frac{T_{sat} - T_{wall}}{d}\, x \qquad (39)$$

With $d = 9\Delta x$ (four cells full of vapor and five mixed cells), which corresponds to the "end" of the interface (see Figure 21) and x the position of the cell centre. Concerning the comparison of the simulation results and the analytical solution, the same observations can be done with the location of the interface and temperature deflection, as shown in Figure 21. The time onset is calculated using the initial computed interface centre position increased by $2.5\Delta x$.

The results are given in Figure 22. Contrary to the sucking problem, the improvement due to the mesh refinement is limited. This result can be explained by the fact that the local temperature gradient at the interface is smaller even if in the whole domain the temperature difference is higher (equal to 25 K versus 5 K in the sucking problem). Figure 19 presents the corresponding average relative error for the interface position for the first 10 s. When the mesh is refined, the error decreases. Thus, a mesh convergence is observed. The order of convergence (using the Richardson's extrapolation (34)) is equal to 0.74.

The sucking and the Stefan problems are interesting test cases since they can be used to calibrate empirical models usually used to deal with phase changes in commercial codes at different pressure and temperature conditions for water/steam flows as an example.

In this paper, two 1D test cases have been used to validate the new heat transfer model considering super-saturated liquid water on the one hand and super-saturated steam on the other hand. The validation has been successfully extended to 3D simulations, under-saturated water and pressure conditions occurring in a reactor vessel or a steam generator of a nuclear power plant [*e.g.*, Fleau 2017].

Conclusion

A multifield approach based on a two-fluid model has been implemented in the CMFD code NEPTUNE_CFD to simulate complex flows containing inclusions with a large range of sizes. This approach has been widely validated in previous papers on laminar isothermal flows. However, turbulence effects with the two-fluid model applied to large and deformable interfaces have never been studied. Thus, the equations have been filtered for the first time. Two specific subgrid terms appeared conducting to a total of seven subgrid terms. The analysis of the weight of each term highlighted that the surface tension subgrid term was predominant, in agreement with previous LES studies on one-fluid models, whereas the diffusive subgrid term could not be negligible. The comparison of turbulence models finally showed that ADM was the most suitable model for all subgrid terms appearing in the filtered equations. Then, LES models were used to predict flow regimes. Better results were observed with LES since RANS approaches underestimated void fractions. The simulation performed with ADM was encouraging. Work has to be done to assess the different modelling choices to improve the

results and also to clarify the sense of filtering the drag terms in the momentum equations. Finally, after investigating turbulence, phase change at large interfaces have been explored. For this purpose, a new heat flux model has been implemented and validated in this paper.

The main perspective of this work concerns the implementation of ADM in two-phase flows with the treatment of interfaces and the implementation of all the subgrid terms. Extensions to three field simulations with phase change effects are expected.

References

Adams, N., and Stolz, S. [2002], A subgrid-scale deconvolution approach for schock capturing, *J. Comput. Phys.*, Vol. 178, Issue 2, pp. 391-426.

Alizadehdakhel, A., *et al.* [2010], CFD modeling of flow and heat transfer in a thermosyphon, *Int. Commun. Heat Mass Transfer*, Vol. 37, Issue 3, pp. 312-318.

Anderson, T. B., and Jackson, R. [1967], Fluid mechanical description of fluidized beds. Equations of motion, *Ind. Eng. Chem. Fundam.*, Vol. 6, Issue 4, pp. 527-539.

Bardina, J. *et al.* [1980], Improved subgrid scale models based on Large Eddy Simulation, *AIAA Paper*, Vol. 80.

Bardina, J. *et al.* [1983], Improved turbulence models based on Large Eddy Simulation of homogeneous, incompressible, turbulent flows, *Tech. rep., Thermosciences Division*, Department of Mechanical Engineering, Standford University.

Bartosiewicz, Y. *et al.* [2008], A first assessment of the NEPTUNE_CFD code: Instabilities in a stratified flow comparison between the VOF method and a two-field approach, *Int. J. Heat and Fluid Flow*, Vol. 29, pp. 460-478.

Bottin, M. *et al.* [2014], Experimental investigation of a developing two-phase bubbly flow in horizontal pipe, *Int. J. Multiphase Flow*, Vol. 60, pp. 161-179.

Brackbill, J. U. *et al.* [1992], A continuum method for modeling surface tension, *J. Comput. Phys.*, Vol. 100, pp. 335-354.

Capecelatro, J. *et al.* [2010], Eulerian-Lagrangian Simulations of Three-Dimensional Turbulent Riser Flows, Proceedings of the 63rd Annual Meeting of the APS Division of Fluid Dynamics, Long Beach, California.

Carrara, M. D., and DesJardin, P. E., [2008], A filtered mass density function approach for modeling separated two-phase flows for LES II: Simulation of a droplet laden temporally developing mixing layer, *Int. J. Multiphase Flow*, Vol. 34, pp. 748-766.

Denèfle, R. *et al.* [2015], Multifield hybrid approach for two-phase flow modeling – Part 1: Adiabatic flows, *Comput. Fluids*., Vol. 113, pp. 106-111.

Drew, D. A., and Lahey, R. T. [1979], Application of general constitutive principles to the derivation of multidimensional two-phase flow equations, *Int. J. Multiphase Flow*, Vol. 5, Issue 4, pp. 243-264.

Duponcheel M. *et al.* [2016], Experimental and Numerical Investigations of a Two-Phase Wavy Flow**,** accepted in *Nucl. Eng. Des*.

Emonot, P. *et al.* [2011], CATHARE-3: a new system code for thermal-hydraulics in the context of the NEPTUNE project, *Nucl. Eng. Des*., Vol. 241, pp. 4476-4481.

Fang, C. *et al.* [2010], Volume Of Fluid simulation of boiling two-phase flow in a vapor-venting microchannel, *Front. Heat Mass Transfer*, Vol. 1, pp. 1-11.

Fleau, S. *et al.* [2015], Validation of a multifield approach for the simulations of two-phase flows, C*omput. Therm. Sci.*, Vol. 7, Issue 5-6, pp. 441-457.

Fleau, S. *et al.* [2016], Study of an interface sharpening method for large interface tracking within a two-fluid model, Proceeding of the 9th International Conference on Multiphase Flow: ICMF 2016, Firenze, Italy.

Fleau, S. [2017], Multifield approach and interface locating method for two-phase flows in nuclear power plant, *PhD Thesis*, University of Paris-Est Marne-la-Vallée, EDF R&D.

Ganapathy, H. *et al.* [2013], Volume Of Fluid-based numerical modeling of condensation heat transfer and fluid flow characteristics in microchannels, *Int. J. Heat Mass Transfer*, Vol. 65, pp. 62-72.

Germano, M. *et al.* [1991], A dynamic subgrid-scale eddy viscosity model, *Phys. Fluids*, Vol. 3, pp. 1760-1765.

Guelfi, A. *et al.* [2007], Neptune - a new software platform for advanced nuclear thermal hydraulics, *Nucl. Sci. Eng*., Vol. 156, pp. 281-324.

Herrmann, M. [2010], A parallel Eulerian interface tracking/Lagrangian point particle multi-scale coupling procedure, *J. Comput. Phys.*, Vol. 229, pp. 745-759.

Hirt, C.W., and Nichols, B.D. [1981], Volume of fluid (VOF) method for the dynamics of free boundaries, *J. Comput. Phys.*, Vol. 39, pp. 201-225.

Ishii, M. [1975], *Thermo-fluid dynamic, theory of two-phase flow*, Eyrolles.

Kunkelmann, C. *et al.* [2012], The effect of three-phase contact line speed on local evaporative heat transfer: experimental and numerical investigations, *Int. J. Heat Mass Transfer*, Vol. 55, pp. 1896-1904.

Labourasse, E. *et al.* [2007], Towards large eddy simulation of isothermal two-phase flows: Governing equations and a priori tests, *Int. J. Multiphase Flow*, Vol. 33, pp. 1-39.

Lakehal, D. [2004], DNS and LES of turbulent multifluid flows, Proceedings of 3rd International Symposium on two-Phase Flow Modelling and Experimentation, Pisa, Italy.

Larocque, J. *et al.* [2010], Parametric study of LES subgrid terms in a turbulent phase separation flow, *Int. J. Heat Fluid Flow*, Vol. 31, pp. 536-544.

Lebas, R. *et al.* [2009], Numerical simulation of primary break-up and atomization: DNS and modelling study, *Int. J. Multiphase Flow*, Vol. 35, Issue 3, pp. 247-260.

Lee, W. [1980], A pressure iteration scheme for two-phase flow modelling, *Multiphase Transport fundamentals, Reactor Safety, Applications, Hemisphere Publishing*.

Ling, Y. *et al.* [2015], Multiscale Simulation of Atomization with Small Droplets Represented by a Lagrangian Point-Particle Model, *Int. J. Multiphase Flow*, Vol. 76, pp. 122-143.

Mao, W. [2009], Numerical simulation of vapor-liquid phase change heat transfer and micromixing in microfluidic systems, *M.Sc. Thesis*, Guangzhou Institute of Energy Conversion, Chinese Academy of Sciences, China.

Mimouni, S. *et al.* [2011], Combined evaluation of second order turbulence model and polydispersion model for two-phase boiling flow and application to fuel assembly analysis, *Nucl. Eng. Des.*, Vol. 241, Issue 11, pp. 4523-4536.

Mimouni, S. *et al.* [2016], Towards a more general CFD modelling for all flow regimes, ICMF2016, Proceeding of the 9th International Conference on Multiphase Flow, Firenze, Italia.

Mimouni, S. *et al.* [2017], CFD calculations of flow pattern maps and LES of multiphase flows, *Nucl. Eng. Des.*, Vol. 321, pp. 118-131.

Nichita, A., and Thome, J. [2010], A Level Set method and a heat transfer model implementation into FLUENT for modeling of microscale two-phase flows, Poceedings of "AVT-178 Specialists" Meeting on System Level Thermal Management for Enhanced Platform Efficiency, No. EPFL-CONF-151629.

Nicoud, F., and Ducros, F. [1999], Subgrid-scale stress modelling based on the square of the velocity gradient tensor, *Flow, Turbul. Combust.*, Vol. 62, Issue 3, pp. 183-200.

Olsson, E., and Kreiss, G. [2005], A conservative Level Set method for two phase flow, *J. Comput. Phys.*, Vol. 210, pp. 225-246.

Patankar, S., and Spalding, D. [1972], A calculation procedure for heat, mass and momentum transfer in three-dimensional parabolic flows, *Int. J. Heat Mass Transf.*, Vol. 15, No. 10, pp. 1787-1806.

Sagaut, P., and Germano, M. [2005], On the filtering paradigm for LES of flows with discontinuities, *J. Turbul.*, Vol. 6, Issue 23.

Sato, Y., and Niceno, B. [2013], A sharp-interface phase change model for a mass-conservative interface tracking method, *J. Comput. Phys.*, Vol. 249, pp. 127-161.

Schepper, S. D. *et al.* [2009], Modeling the evaporation of a hydrocarbon feedstock in the convection section of a steam cracker, *Comput. Chem. Eng.*, Vol. 33, pp. 122-132.

Schlatter, P. *et al.* [2004], LES of transitional flows using the approximate deconvolution model, *Int. J. Heat Fluid Fl.*, Vol. 25, Issue 3, pp. 549-558.

Smagorinsky, J. [1963], General circulation experiments with the primitive equations, *Monthly Weather Review*, Vol. 91, pp. 99-165.

Štrubelj, L. [2009], Numerical simulations of stratified two-phase flows with two-fluid model and interface sharpening, *M.Sc. Thesis*, University of Ljublana.

Sun, D. *et al.* [2014], Modeling of the evaporation and condensation phase-change problems with FLUENT, *Numer. Heat Transfer*, Part B, Vol. 66, pp. 326-342.

Sussman, M. *et al.* [1994], A level set approach for computing solutions to incompressible two-phase flow, *J. Comput. Phys.*, Vol. 114, pp. 146-159.

Tomar, G. *et al.* [2010], Multiscale simulations of primary atomization, *Comput. Fluids*, Vol. 39, Issue 10, pp. 1864-1874.

Tavares, M. *et al.* [2016], A priori study for the modeling of LES subgrid scale terms, Proceedings of the 4th Turbulence and Interactions conference TI2015, Cargèse, France.

Trontin, P. *et al.* [2012], A phase-conditioned filtering of incompressible interfacial multiphase flow equations: A Priori study for the modeling of LES subgrid scale terms, Proceedings of Turbulence and Interactions, La Saline-les-Bains, La Réunion, France.

Unverdi, S.O., and Tryggvason, G. [1992], A front-tracking method for viscous, incompressible, multi- fluid flows, *J. Comput. Phys.*, Vol. 10, pp. 25-37.

Vallet, A., and Borghi, R. [1999], Modélisation Eulérienne de L'atomisation d'un Jet Liquide, *C. R. Acad. Sci. Paris*, Série IIb, Vol. 327, Issue 10, pp. 1015-1020.

Vincent, S. *et al.* [2008], Numerical simulation of phase separation and a priori two-phase LES filtering, *Comput. Fluids*, Vol. 37, Issue 7, pp. 898-906.

Vincent, S. *et al.* [2016], *A priori* filtering and LES modeling of turbulent two-phase flows application to phase separation, *accepted in Comput. Fluids*.

Welch, S., and Wilson, J. [2000], A Volume Of Fluid based method for fluid flows with phase change, *J. Comput. Phys.*, Vol. 160, pp. 662-682.

Wu, H. *et al.* [2007], Simulation of refrigerant flow boiling in serpentine tubes, *Int. J. Heat Mass Transfer*, Vol. 50, pp. 1186-1195.

Yang, Z. *et al.* [2008], Numerical and experimental investigation of two-phase flow during boiling in a coiled tube, *Int. J. Heat Mass Transfer*, Vol. 51, Issue 5, pp. 1003-1016.

Zuzio, D. *et al.* [2013], Numerical simulation of primary and secondary atomization, *C. R. Mecanique*, Vol. 241, pp. 15-25.

Subgrid terms	Expressions
τ_{interf}	$\rho_k\left(\nabla.\left(\overline{\varepsilon_k^* u_{i,k}}\right) - \nabla.\left(\overline{\varepsilon_k^*}\ \overline{u_{i,k}}\right)\right)$
τ_{time}	$\rho_k\left(\partial_t\left(\overline{\varepsilon_k^* u_{i,k}}\right) - \partial_t\left(\overline{\varepsilon_k^*}\ \overline{u_{i,k}}\right)\right)$
τ_{conv}	$\rho_k\left(\nabla.\left(\overline{\varepsilon_k^*\, u_{i,k} u_{j,k}}\right) - \nabla.\left(\overline{\varepsilon_k^*}\ \overline{u_{i,k}}\ \overline{u_{j,k}}\right)\right)$
τ_{diff}	$\mu_k\left(\nabla.\left(\overline{\varepsilon_k^* S_k}\right) - \nabla.\left(\overline{\varepsilon_k^*}\ \overline{S_k}\right)\right)$
$\tau_{pressure}$	$\overline{\alpha_k \nabla P} - \overline{\alpha_k} \nabla \overline{P}$
τ_{superf}	$\sigma\left(\overline{\varepsilon_k^* \kappa \nabla \alpha_k} - \overline{\varepsilon_k^*}\ \hat{\kappa}\ \nabla \overline{\alpha_k}\right)$

Table 1. *Expression of the subgrid terms appearing in the filtered two-fluid equations,* $\hat{\kappa} = -\nabla.\left(\frac{\nabla\overline{\varepsilon_k^*}}{\left\|\nabla\overline{\varepsilon_k^*}\right\|}\right)$ *being the filtered local curvature*

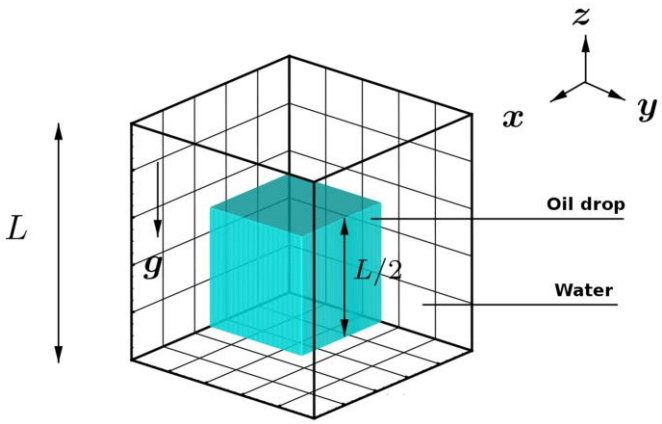

Figure 1. *Initial conditions of the phase inversion benchmark.*

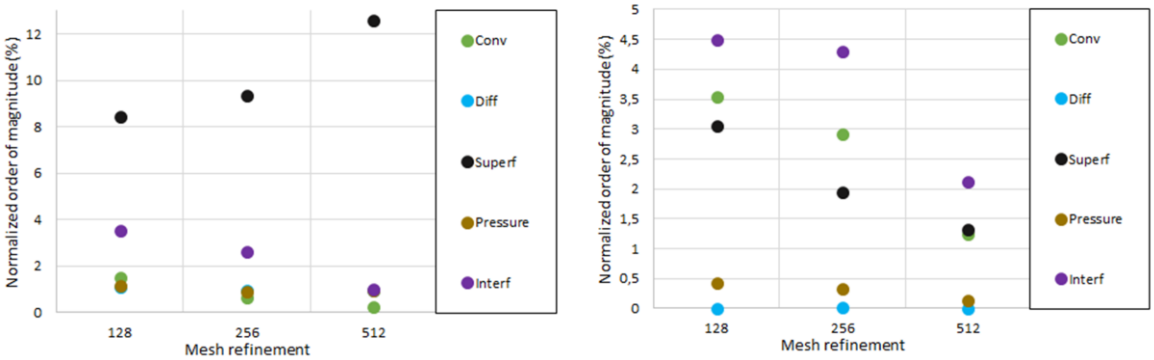

Figure 2. *Order of magnitude of the normalized subgrid terms, left: for the oil phase, right: for the water phase, only the z component is displayed.*

Phase	ρ (kg.m^{-3})	μ (kg.m^{-1}.s^{-1})
Oil	900	0.1
Water	1000	$1 \cdot 10^{-3}$

Table 2. *Physical properties of the two phases in the phase inversion benchmark*

	Oil	Water
1	τ_{superf}	τ_{superf}
2	$\tau_{pressure}$	τ_{conv}
3	τ_{diff}	$\tau_{pressure}$
4	τ_{conv}	τ_{interf}
5	τ_{interf}	τ_{diff}

Table 3. *Classification of the subgrid terms according to their relative contribution for the 512^3 grid with the box filter*

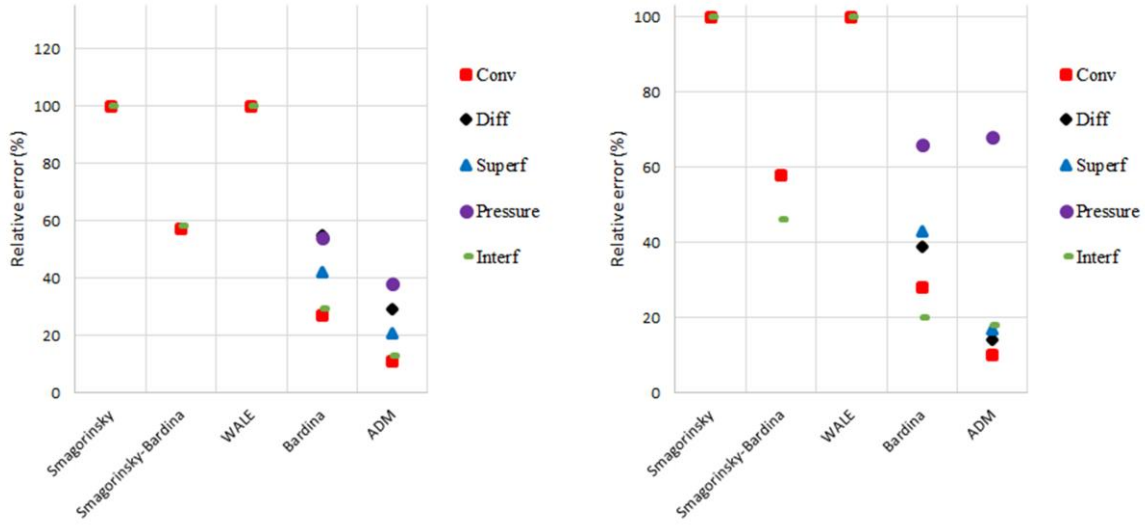

Figure 3. *Relative error obtained by comparison between the modeled subgrid term and the terms obtained by DNS, left: for the oil phase, right: for the water phase, only the z component is displayed, mesh with 512^3 cells.*

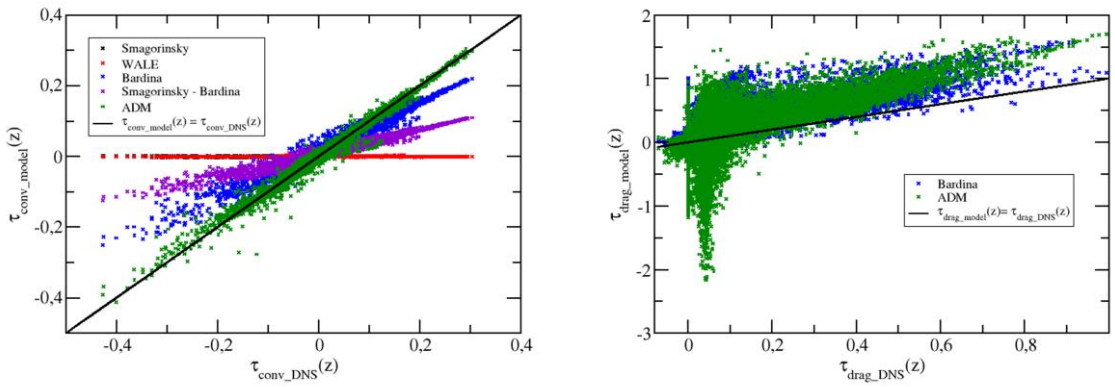

Figure 4. *Correlation between the turbulence models and the subgrid terms evaluated by DNS, left: convective subgrid term, right: drag subgrid term in the intermediate region $0.3 \leq \varepsilon_2^* \leq 0.7$, only the component in the z direction is considered, mesh with 128^3 cells, oil phase.*

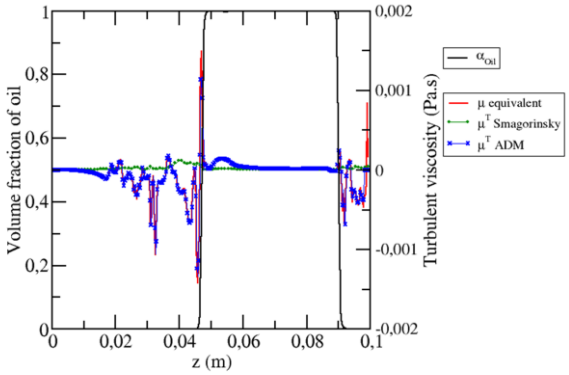

Figure 5. *Comparison of the equivalent viscosity μ_{eq} predicted by DNS and the turbulent viscosity obtained with the Smagorinsky's model and ADM, the volume fraction of oil is also represents to locate interfaces, the viscosities are extracted from a slice of the domain at x = y = 8 cm, mesh with 512^3 cells.*

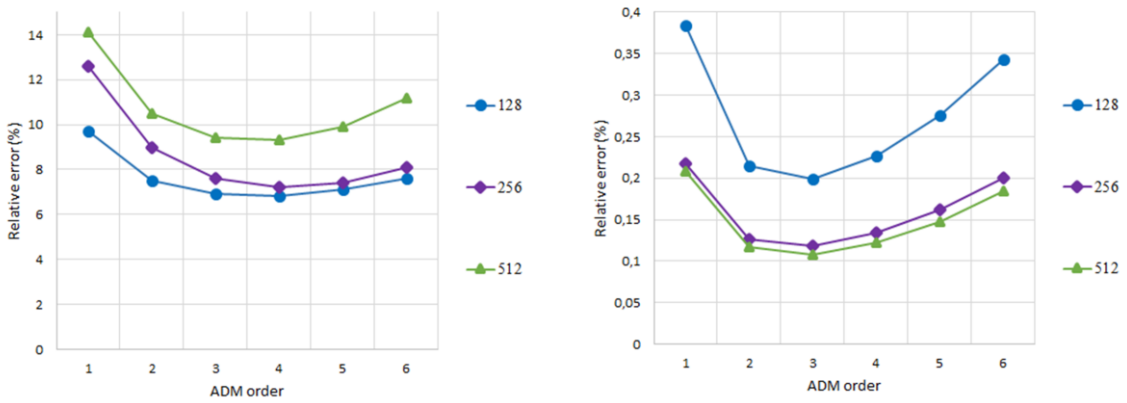

Figure 6. *Relative error of the convection subgrid term (left) and the predicted velocity field (right) according to the ADM order for the three grids and the oil phase.*

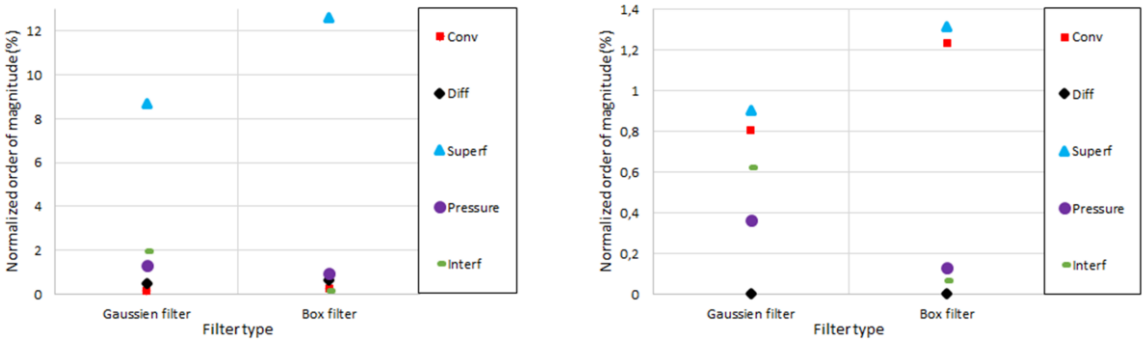

Figure 7. *Order of magnitude of the normalized subgrid terms obtained with the box and the Gaussian filter, left: for the oil phase, right: for the water phase, only the z component is displayed, mesh with 512^3 cells.*

LES filter		
	Oil	**Water**
1	τ_{superf}	τ_{superf}
2	τ_{interf}	τ_{conv}
3	$\tau_{pressure}$	τ_{interf}
4	τ_{diff}	$\tau_{pressure}$
5	τ_{conv}	τ_{diff}

Table 4. *Classification of the subgrid terms according to their relative contribution for the 512^3 grid with the Gaussian filter*

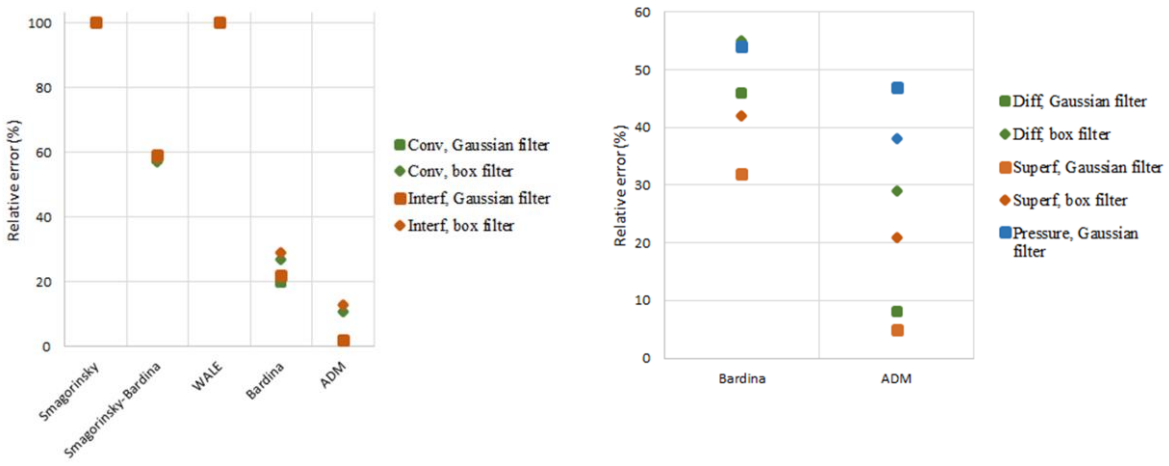

Figure 8. *Relative error obtained by comparison between the modeled subgrid term and the terms obtained by DNS with the box and the Gaussian filters, for the oil phase with the 512^3 grid, only the z component is displayed.*

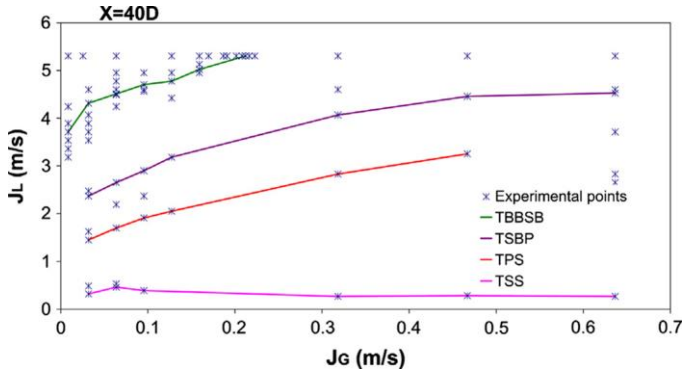

Figure 9. *METERO flow pattern at X = 40 D, J_L corresponds to the water velocity and J_G to the air velocity at the injection, TSS refers to the transition from slug to stratified flow (pink line), TPS to the transition from plug to slug flow (orange line), TBBSB to the transition from buoyant bubble flow to stratified bubble flow (green line) and TSBP to the transition from stratified bubbles regime to plug (purple line), crosses correspond to video acquisitions [e.g., Bottin et al. 2014].*

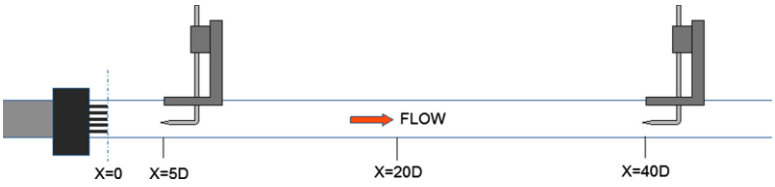

Figure 10. *Schematic view of the horizontal pipe of the METERO experiment [e.g., Bottin et al. 2014].*

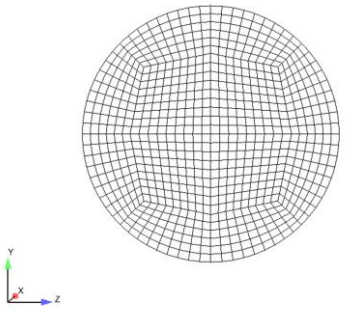

Figure 11. *Slice of the mesh used for the simulation of the METERO test case.*

Phase	ρ (kg.m^3)	μ (kg.m^{-1}.s^{-1})
Air	1.29	$1.8 \cdot 10^{-5}$
Water	1000	$1.3 \cdot 10^{-3}$

Table 5. *Physical properties of the two phases in the METERO test case*

Flow regime	RANS	WALE
Dispersed bubble flow	0.5 ms	0.5 ms
Plug flow	0.25 ms	0.2 ms
Slug flow	0.12 ms	0.12 ms

Table 6. *Time steps according to the flow regime and the turbulence model for the METERO test case*

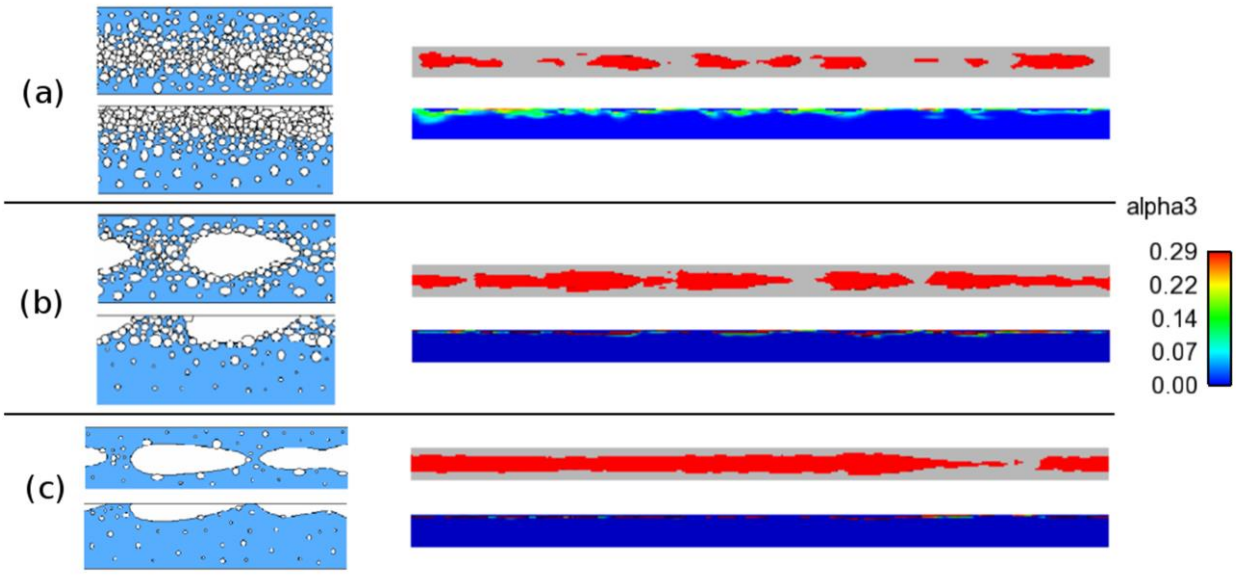

Figure 12. *Qualitative comparison of the simulations performed with the WALE model, (a) stratified bubble flow (J_L = 4.42 m.s^{-1}), (b) plug flow (J_L = 2.65 m.s^{-1}), (c) slug flow (J_L = 1.59 m.s^{-1}), J_G = 0.127 m.s^{-1}, left column: schematic view of the expected flow regime (top view and side view), right column: simulation results, top: top view of the isosurface of the continuous gas field, bottom: volume fraction of the dispersed gas field.*

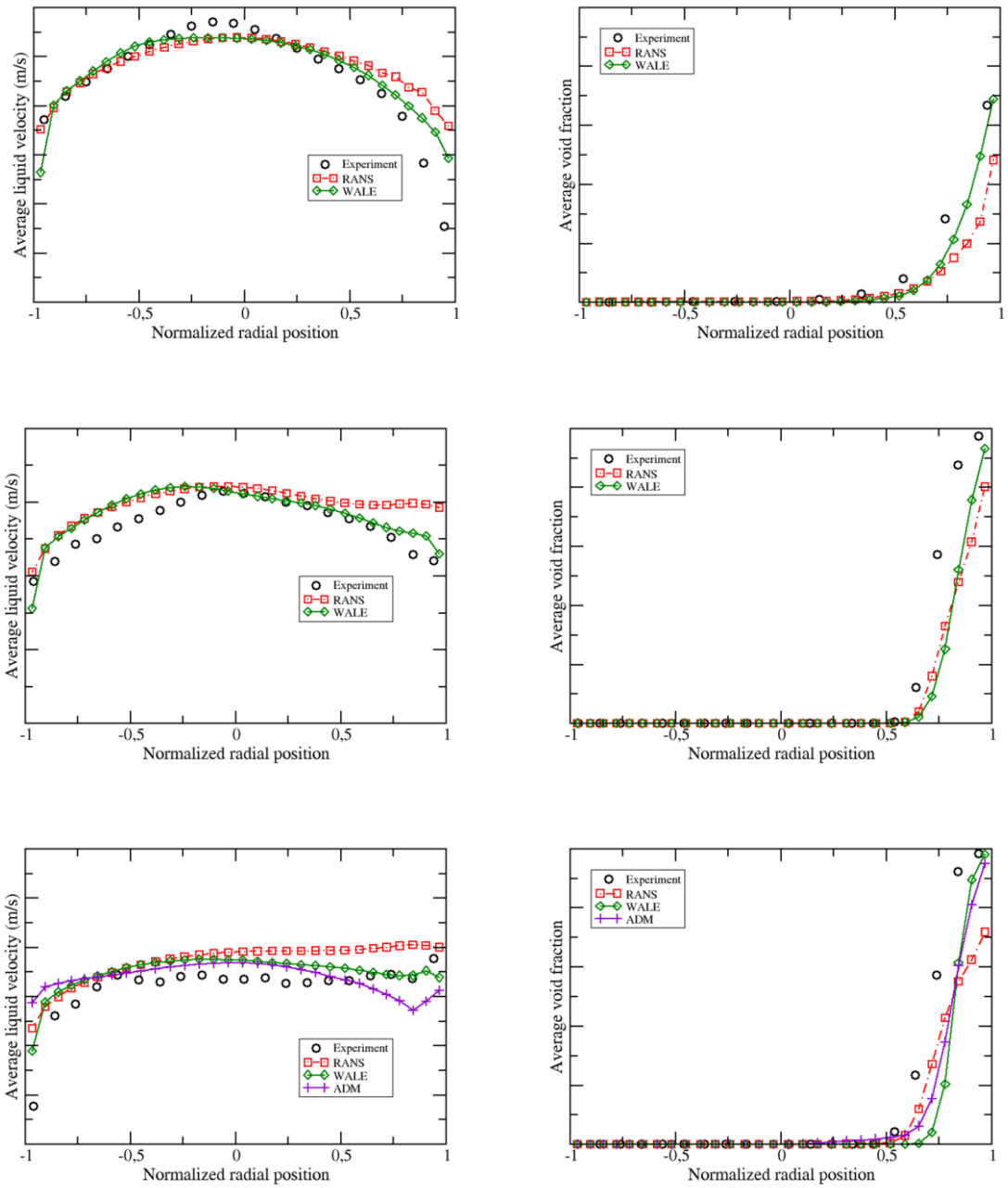

Figure 13. *Average liquid velocity and average void fraction at X = 40D, top to bottom: stratified bubble flow (J_L = 4.42 m.s^{-1}), plug flow (J_L = 2.65 m.s^{-1}), slug flow (J_L = 1.59 m.s^{-1}), J_G = 0.127 m.s^{-1}.*

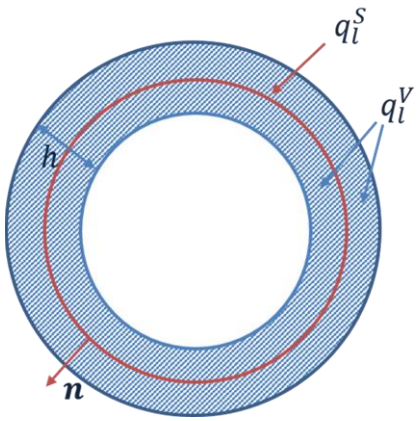

Figure 14. *Notations for the implementation of the new heat flux model, red circle: interface with a zero thickness, blue ring: interface with a non-zero thickness.*

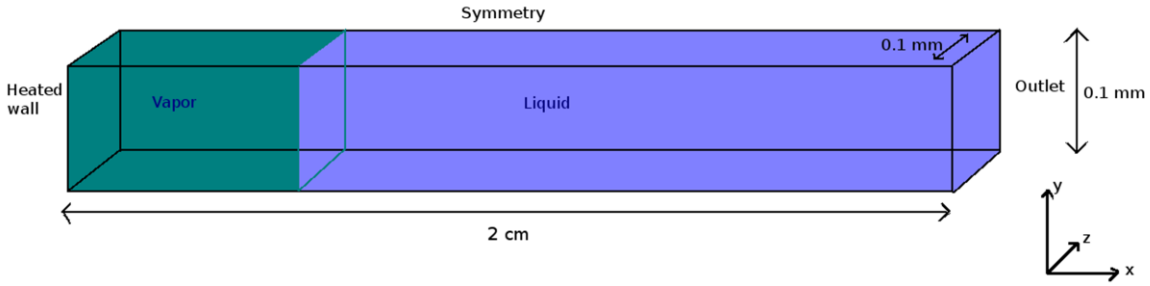

Figure 15. *Definition sketch of the 1D computational domain used for the simulation of the sucking and the Stefan problems.*

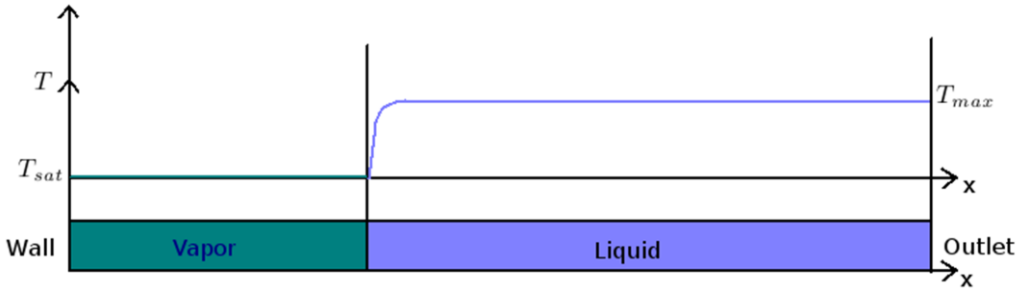

Figure 16. *Simulation conditions at a given time for the sucking problem, the liquid boils and the interface moves to the right side due to volume expansion of the liquid-vapor phase change.*

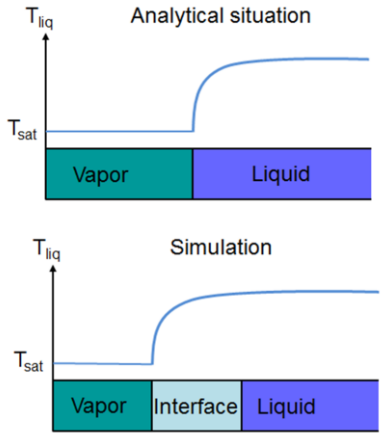

Figure 17. *Schematic view of the temperature profile and vapor/liquid interface in the analytical test case (top) and the simulation (bottom), sucking problem.*

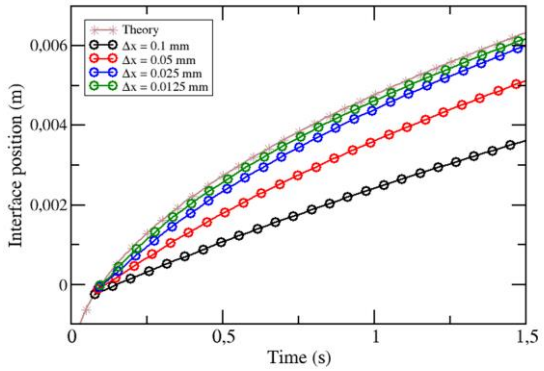

Figure 18. *Evolution of the interface position obtained with the new heat transfer model and different mesh refinements, sucking problem at an atmospheric pressure.*

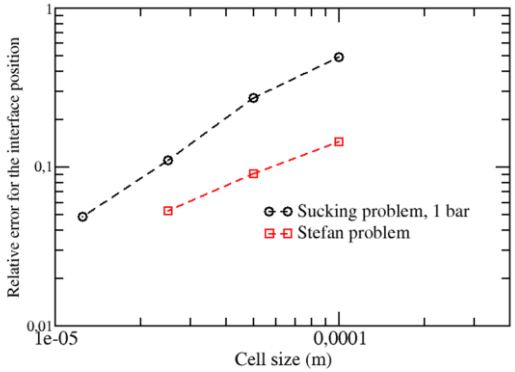

Figure 19. *Average relative error for the interface position compared to the theoretical results obtained with the new heat flux model for the two test cases presented in this paper.*

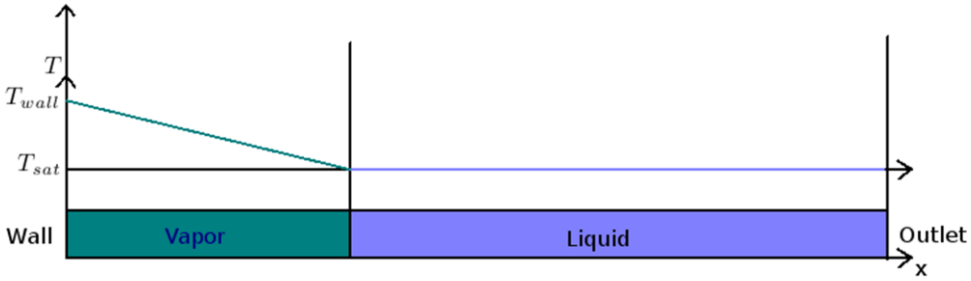

Figure 20. *Simulation conditions at a given time for the Stefan problem, the liquid boils and the interface moves to the right side due to volume expansion of the liquid-vapor phase change.*

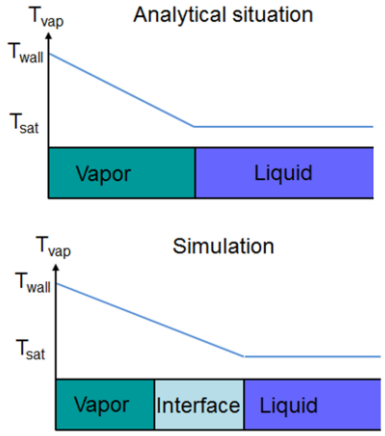

Figure 21. *Schematic view of the temperature profile and vapor/liquid interface in the analytical test case (top) and the simulation (bottom), Stefan problem.*

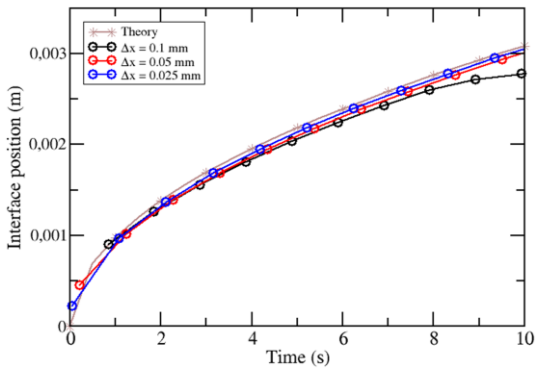

Figure 22. *Evolution of the interface position obtained with the new heat transfer model and different mesh refinements, Stefan problem at an atmospheric pressure.*